PAPER • OPEN ACCESS

Silicon photonics-integrated time-domain balanced homodyne detector for quantum tomography and quantum key distribution

To cite this article: Yanxiang Jia *et al* 2023 *New J. Phys.* **25** 103030

View the article online for updates and enhancements.

New Journal of Physics
The open access journal at the forefront of physics

PAPER

Silicon photonics-integrated time-domain balanced homodyne detector for quantum tomography and quantum key distribution

Yanxiang Jia[1,2], Xuyang Wang[1,2,3,*], Xiao Hu[4,5], Xin Hua[4,5], Yu Zhang[1,2], Xubo Guo[1,2], Shengxiang Zhang[5], Xi Xiao[4,5,*], Shaohua Yu[4,5], Jun Zou[6] and Yongmin Li[1,2,3,*]

1. State Key Laboratory of Quantum Optics and Quantum Optics Devices, Institute of Opto-Electronics, Shanxi University, Taiyuan 030006, People's Republic of China
2. Collaborative Innovation Center of Extreme Optics, Shanxi University, Taiyuan 030006, People's Republic of China
3. Hefei National Laboratory, Hefei 230088, People's Republic of China
4. State Key Laboratory of Optical Communication Technologies and Networks, China Information and Communication Technologies Group Corporation (CICT), Wuhan 430074, People's Republic of China
5. National Information Optoelectronics Innovation Center, Wuhan 430074, People's Republic of China
6. ZJU-Hangzhou Global Scientific and Technological Innovation Center, Zhejiang University, Hangzhou 311215, People's Republic of China
* Authors to whom any correspondence should be addressed.

E-mail: wangxuyang@sxu.edu.cn, xxiao@wri.com.cn and yongmin@sxu.edu.cn

Abstract

We designed and experimentally demonstrated a silicon photonics-integrated time-domain balanced homodyne detector (TBHD), containing an optical part of dimensions of $1.5\,\text{mm} \times 0.4\,\text{mm}$. To automatically and accurately balance the detector, new variable optical attenuators were used, and a common mode rejection ratio of 86.9 dB could be achieved. In the quantum tomography experiment, the density matrix and Wigner function of a coherent state were reconstructed with 99.97% fidelity. The feasibility of this TBHD in a continuous-variable quantum key distribution (CVQKD) system was also demonstrated. Our TBHD technologies are expected to be used in silicon photonics-integrated CVQKD system and silicon photonics-integrated BB84 heterodyne system.

1. Introduction

Time-domain balanced homodyne detectors (TBHDs) are crucial components in quantum information fields, such as quantum tomography and continuous-variable quantum key distribution (CVQKD) [1–17]. These detectors can be used to measure the quadratures of pulsed quantum signals. Furthermore, TBHDs are compatible with photon counting technology. Thus, the TBHD can be used to detect pulsed signal beams with an intensity of approximately several photons or can act as photon counters [18–20]. Conventionally, TBHDs are fabricated using free-space optical devices or fiber optical devices [21, 22]. With considerable developments in quantum information and large-scale optical integration technology, realizing the conventional functions of TBHD on an integrated platform is imperative [23–39].

Recently, frequency-domain balanced homodyne detectors (FBHDs) integrated on silicon photonics chips have been reported [40, 41]. These studies focused on the bandwidth of the detectors. However, TBHDs (use charge and shaping amplifiers), are different from FBHDs (use a transimpedance amplifier) [21, 22, 42, 43]. In the study, we designed and experimentally demonstrated a silicon photonics-integrated TBHD. The technical challenge to realize TBHD is achieving a high common mode rejection ratio (CMRR), which is larger than 70–80 dB. Here, the optical intensities and paths of both outputs of the 50/50 coupler are equal, and the response of the two photodiodes to the pulsed beam are matched [21, 22]. In our study, to realize a well-performing TBHD on a chip, several methods were employed and demonstrated. First, variable optical attenuators (VOAs) without Mach–Zehnder interferometer (MZI) structures and low insertion loss are employed to tune the balance of a 50/50 multimode interference (MMI) coupler. The VOAs are based on the

p–i–n phase modulator, and the principle of attenuation is free carriers absorption. The insertion loss of one VOA was approximately 0.1 dB, which was less than that of the MZI structures. Second, edge couplers were used to achieve a lower coupling loss instead of vertical grating couplers. Third, optical paths after the 50/50 MMI coupler are equal. It is more convenient to realize equal optical paths on a chip than using free-space or fiber optical devices. Finally, we find that the photodiodes on the same wafer can match well with each other and a higher CMRR of 86.9 dB can be achieved. Thus, the selection of matched photodiodes is not necessary.

To further demonstrate the performance of the silicon photonics-integrated TBHD, typical quantum tomography and CVQKD experiments were designed and realized. In quantum tomography, the density matrix and Wigner function of the coherent state $|\alpha\rangle = 1.04$ was reconstructed with 99.97% fidelity using the maximum likelihood method. In the CVQKD experiment, when the transmission channel was 5 dB loss, 10 dB loss, and 50 km fiber, the excess noise could be controlled to approximately 0.029 ± 0.009, 0.077 ± 0.012, and 0.096 ± 0.049, respectively. The performance of chip-based TBHD in evaluating the excess noise was similar to that of the fiber-based TBHD, except for the detection efficiency. Recently, it is reported that the BB84 protocol, which was proposed by Bennett and Brassard in 1984 [44], can be implemented with heterodyne detection instead of single photon detection. Then, the receiver's whole optical devices can be realized on one silicon photonics chip [45, 46]. It is expected that the proposed TBHD technologies can be used in the silicon photonics-integrated CVQKD system and silicon photonics-integrated BB84 heterodyne system.

In section 2, the structure and characteristics of the silicon photonics-integrated TBHD are presented. Moreover, the VOAs are characterized in detail. In section 3, a quantum tomography experiment based on the silicon photonics-integrated TBHD is demonstrated. In section 4, the CVQKD experiments using GG02 protocol, which was proposed by Grosshans and Grangier [6], are demonstrated with the silicon photonics-integrated TBHD. Finally, section 5 presents the conclusion.

2. Structure and characteristics of silicon photonics-integrated TBHD

The schematic diagram of TBHD is shown in figure 1(a). The signal pulse $\hat{a}_S$ and local oscillator (LO) pulse $\hat{a}_L$ interfere at a 50/50 coupler, and the output beams $\hat{c}$ and $\hat{d}$ are guided into two photodiodes with detection efficiency η. The total number of subtracted photoelectrons $\hat{\Delta}$ can be described by

$$\hat{\Delta} = \eta \cdot |\beta| \cdot \hat{X}_\phi + \sqrt{(1-\eta)\eta/2} \cdot |\beta| \cdot \left(\hat{X}_{vc} + \hat{X}_{vd}\right). \tag{1}$$

Here we have treated the strong LO beam as classical field $\hat{a}_L \approx |\beta| \, e^{i\phi}$, where $|\beta|$ represents the amplitude of the LO beam and ϕ is the phase of the LO beam. $\hat{X}_{vc}$ and $\hat{X}_{vd}$ are quadratures of vacuum beam introduced by the detection efficiency η of the photodiodes. $\hat{X}_\phi$ is the rotated quadrature operator and is defined as

$$\hat{X}_\phi = \hat{X}\cos\phi + \hat{Y}\sin\phi, \tag{2}$$

where $\hat{X} = \hat{a}_S + \hat{a}_S^\dagger$ and $\hat{Y} = i(\hat{a}_S^\dagger - \hat{a}_S)$ are the quadratures of the signal beam. The subtracted photoelectrons $\hat{\Delta}$ are amplified by the low noise charge amplifier and low noise shaping amplifier. The peak value $\hat{U}_{peak}$ of the output voltage is given by

$$\hat{U}_{peak} = G \cdot \int_0^t \hat{i}(\tau)\mathrm{d}\tau = G \cdot \hat{\Delta}, \tag{3}$$
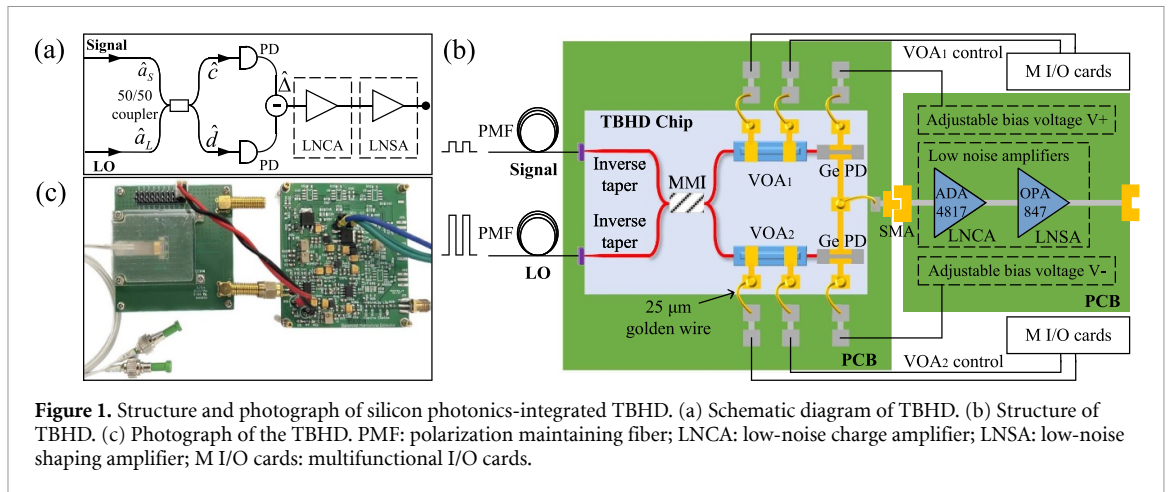
where G is the gain of TBHD and t is the pulse duration, $\hat{i}(\tau)$ is the instantaneous subtracted photoelectrons current with the duration time t. The mean peak value $\langle \hat{U}_{peak} \rangle$ of the output voltage can be described by

$$\langle \hat{U}_{peak} \rangle = G \cdot \langle \hat{\Delta} \rangle = G\eta|\beta|\langle \hat{X}_\phi \rangle. \tag{4}$$

It means that the mean peak value has a linear relationship with the mean quadrature of the pulsed signal field. When the signal beam $\hat{a}_S$ is in vacuum, the mean peak value of output voltage is zero and the variance of the peak value σ^2 becomes

$$\sigma^2 = G^2 \cdot \eta \cdot |\beta|^2. \tag{5}$$

The schematic diagram of silicon photonics-integrated TBHD is presented in figure 1(b). The chip was fabricated using industry-standard active flow silicon-on-insulator (SOI) technology. Moreover, it was based on an SOI substrate with a 3 μm buried oxide layer and 220 nm top silicon. The overall size of the optical part on a chip was 1.5 mm $\times$ 0.4 mm, which was much smaller than the fiber-based TBHD. Since the

Figure 1. Structure and photograph of silicon photonics-integrated TBHD. (a) Schematic diagram of TBHD. (b) Structure of TBHD. (c) Photograph of the TBHD. PMF: polarization maintaining fiber; LNCA: low-noise charge amplifier; LNSA: low-noise shaping amplifier; M I/O cards: multifunctional I/O cards.

quantum signal is very sensitive to detection loss, edge coupling was used to couple the light into the chips instead of vertical coupling using a one-dimensional grating coupler [23]. The signal and LO beams were coupled into the chip through inverse taper array on the edge of the chip. The guided polarization maintaining fibers with high numerical aperture values (NA = 0.4) were packaged on the edge of the chip, and the mode field diameter was around $4.2 \pm 0.3\,\mu$m. The size of the inverse taper tip was approximately 140 nm × 220 nm, and the mode field diameter was around $4.5\,\mu$m, which was matched with that of the high numerical aperture polarization maintaining fiber. Subsequently, an edge coupler loss of 2 dB was achieved using packaged technology. In the chip, the signal and LO beams transmitted in transverse electric mode and interfered with each other in a 50/50 MMI coupler. To balance the intensities of two output paths of the 50/50 MMI coupler, two VOAs based on p–i–n phase modulators were used, which introduces excess losses owing to the free carrier absorption effect when forward voltage was applied. The insertion loss is 0.1 dB when no voltage was applied. At the end of the two output paths, two Ge photodiodes were utilized to detect the interfered beams. The responsivity was $0.9\,\text{A W}^{-1}$, and the dark current was 64 nA at 3.7 V. To balance the optical paths of the two output paths, the lengths of the two output waveguides of the 50/50 MMI coupler were designed to be the same. The bias voltage of two Ge photodiodes were tunable to ensure that the responses of the two photodiodes were identical. Based on the above methods, the pulsed photoelectrons of two Ge photodiodes could be subtracted sufficiently, and a high CMRR could be achieved.

The low-noise charge and shaping amplifiers following the chip are critical to ensure that the TBHD operates at a low electronic noise level and the output pulse is Gaussian [21, 22]. The Op Amps ADA4817 served as the low-noise charge amplifier to integrate the subtracted photoelectrons. For the low-noise shaping amplifier, OPA847 was selected for its high bandwidth. The filters in shaping amplifier can be used to tune the output pulse width of TBHD. Further details about the electronic circuits can be found in [21, 22]. The whole setup was enclosed in a metal box to shield from electromagnetic interference which will introduce large and unstable electronic noise.

To balance the TBHD and achieve a high CMRR, two VOAs based on p–i–n phase modulators were employed instead of the MZI structures. The details about balancing with MZI structures can be seen in the contents of appendix A. Here, the attenuation characteristics of the VOAs based on phase modulators were analyzed in detail. Figure 2(a) depicts the normalized output intensities *I* versus the applied forward voltages on the VOAs. The solid blue square and red triangle lines represent the normalized output intensities of the two VOAs, and the hollow blue square and red triangle lines are the corresponding voltage–current attribution lines. The maximum attenuated amplitude was >80%, and the corresponding current was approximately 9.5 mA, which is below the damage threshold of approximately 10 mA. Generally, the ratio of a 50/50 MMI coupler is extremely close to 50/50 and the attenuated amplitude was enough to compensate for the imbalance of the two output paths of the 50/50 MMI coupler, which has a typical imbalance level of <3% [23]. Hence, a shorter p–i–n could be employed to achieve a lower insertion loss.

In the experiment, suitable voltage resolution ΔV_{vr} and tuning precision ΔI_{tp} are needed to precisely attenuate the normalized output intensity. It is depended on the photoelectron number per pulse $\eta \cdot |\beta|^2$ or shot noise to electronic noise ratio (SENR). The details for estimating ΔV_{vr} and ΔV_{vr} can be seen in appendix B. Here, the required resolution and precision values are listed at different SENRs for VOA_1 in table 1. The parameters of VOA_2 are similar. From table 1, it can be observed that a higher tuning precision is needed when the SENR or photoelectron number per pulse is higher. The needed voltage resolution depends on the region of the points in figure 2(a). The values of points can be seen in the table B1 of appendix B. When the applied voltage is higher, the attenuated normalized output intensity is larger and a higher voltage
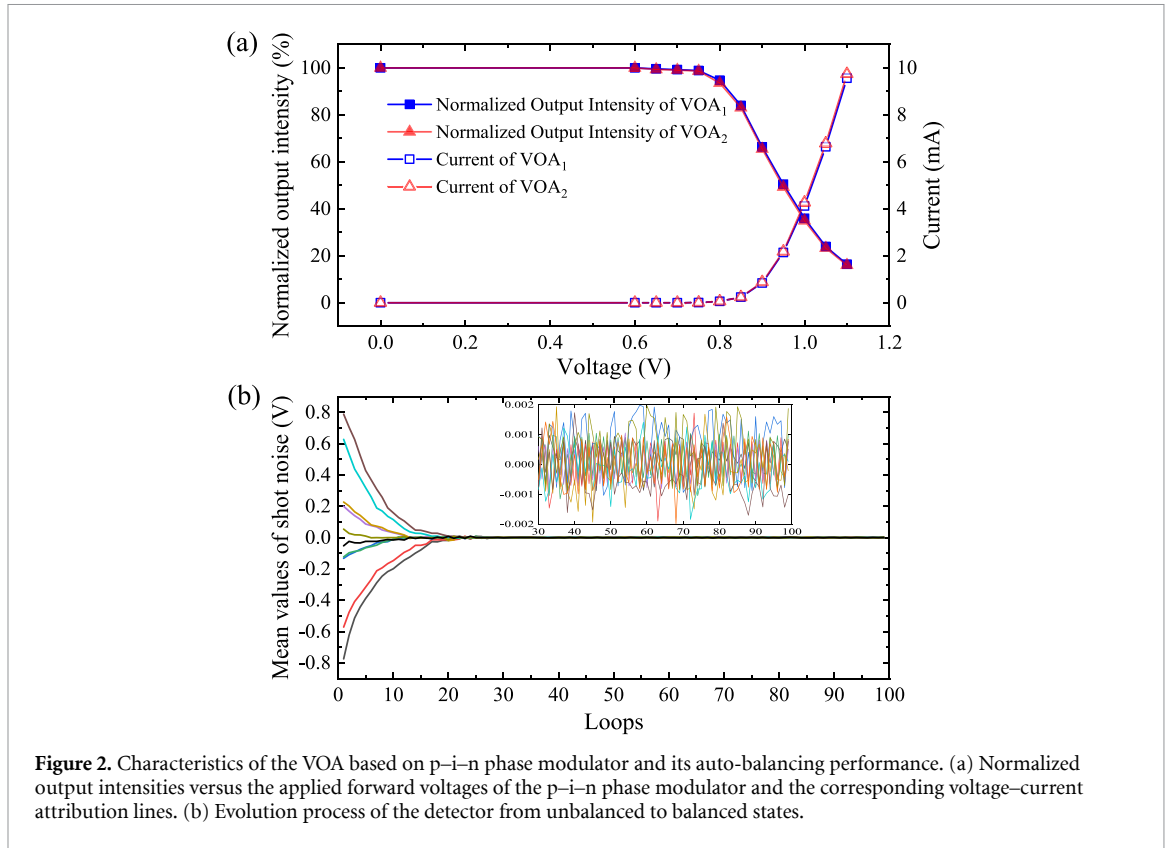
Figure 2. Characteristics of the VOA based on p–i–n phase modulator and its auto-balancing performance. (a) Normalized output intensities versus the applied forward voltages of the p–i–n phase modulator and the corresponding voltage–current attribution lines. (b) Evolution process of the detector from unbalanced to balanced states.

Table 1. Voltage resolution and tuning precision at different SENR.

			Regions between ith and $(i+1)$th points			
			$i=3$		$i=5$	
SENR (dB)	$\eta \cdot \|\beta\|^2$	ΔI_{tp}	$1-I_{i+1}$ (%)	ΔV_{vr} (mV)	$1-I_{i+1}$ (%)	ΔV_{vr} (mV)
5	2.28×10^6	6.62×10^{-4}		11.03		0.78
10	4.55×10^6	4.68×10^{-4}	0.7	7.81	5.3	0.55
15	1.27×10^7	2.65×10^{-4}		4.42		0.31

resolution is needed. In the region between the 5th and 6th points, the maximum attenuated normalized output intensity $1-I_6$ is 5.3% which is larger than the imbalance level of 50/50 MMI. Furthermore the minimum voltage resolution is 0.31 mV when the SENR is 15 dB. The multifunction I/O card USB6259 with a 16 bit digital analog converter was utilized to apply the voltage. When the output range is ± 5 V, a high output voltage resolution of 0.15 mV, which is less than the above required voltage resolutions presented in table 1, can be achieved. It is enough to tune the TBHD into a well balanced state.

Although there is no MZI structure in the proposed TBHD, the output shot noise mean value still drifts due to the 50/50 MMI coupler. Thus, this study designed a simple auto-balancing technique to enable the TBHD steadily run for a long time using the monotonous excess loss-voltage curve. The results are shown in figure 2(b). Approximately 20 loops were required from any initial unbalanced state to the balanced state. When the intensities of two output paths of the 50/50 MMI coupler were balanced, the mean values of the shot noise could be controlled in the ± 2 mV range. Due to the bandwidth of p–i–n phase modulator is 30 MHz, a higher speed control than MZI structures based thermal phase shifter whose bandwidth is about tens of kHz can be achieved. The auto-balancing processes can be seen in appendix C in detail.

With the above auto-balancing technique, the oscilloscope (Tektronix MSO 5204B) traces of the output shot noise are shown in figure 3(a). Here, the oscilloscope sampling rate is 2 GHz; voltage range is ± 0.25 V, the analog-to-digital converter is eight bit; and the voltage resolution is 1.95 mV. The wavelength of input pulsed laser beam is 1550.14 nm, and the pulse width is 100 ns. The setup of generating the pulsed laser beam can be seen in section 3 in detail. The output electric pulse repetition rate is 1 MHz, and the pulse width is approximately 200 ns. The measured photoelectron number of the two photodiodes is 1.42×10^7, and the SENR is 15 dB. A CMRR of 86.9 dB could be measured. The detailed measurement method of CMRR of TBHD is shown in appendix B. In comparison to the TBHD with commercial InGaAs photodiodes, selecting
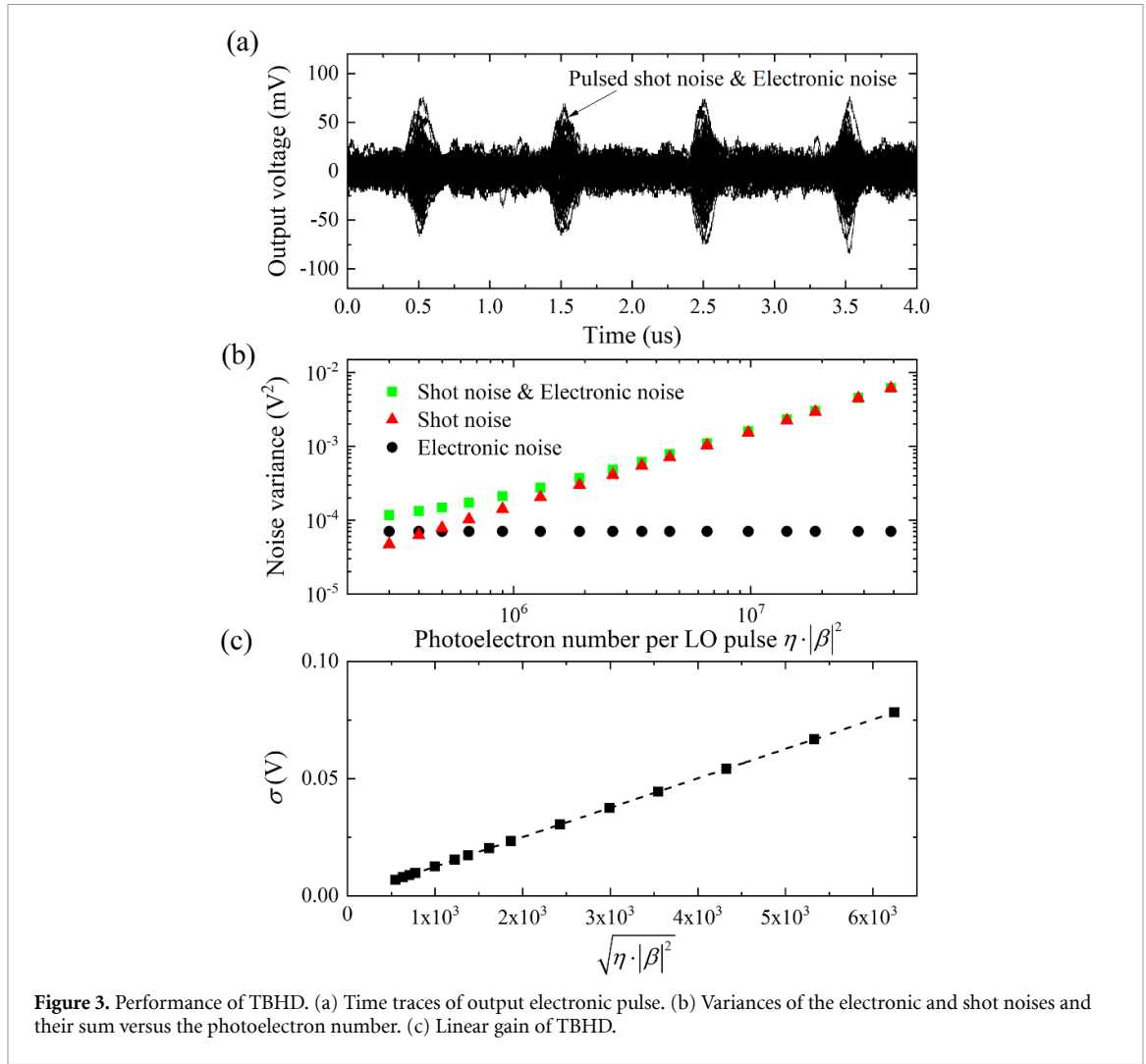
Figure 3. Performance of TBHD. (a) Time traces of output electronic pulse. (b) Variances of the electronic and shot noises and their sum versus the photoelectron number. (c) Linear gain of TBHD.

the matched photodiodes was unnecessary. We infer that the two Ge photodiodes were fabricated in the same wafer using the same procedures; therefore, they exhibited a similar performance.
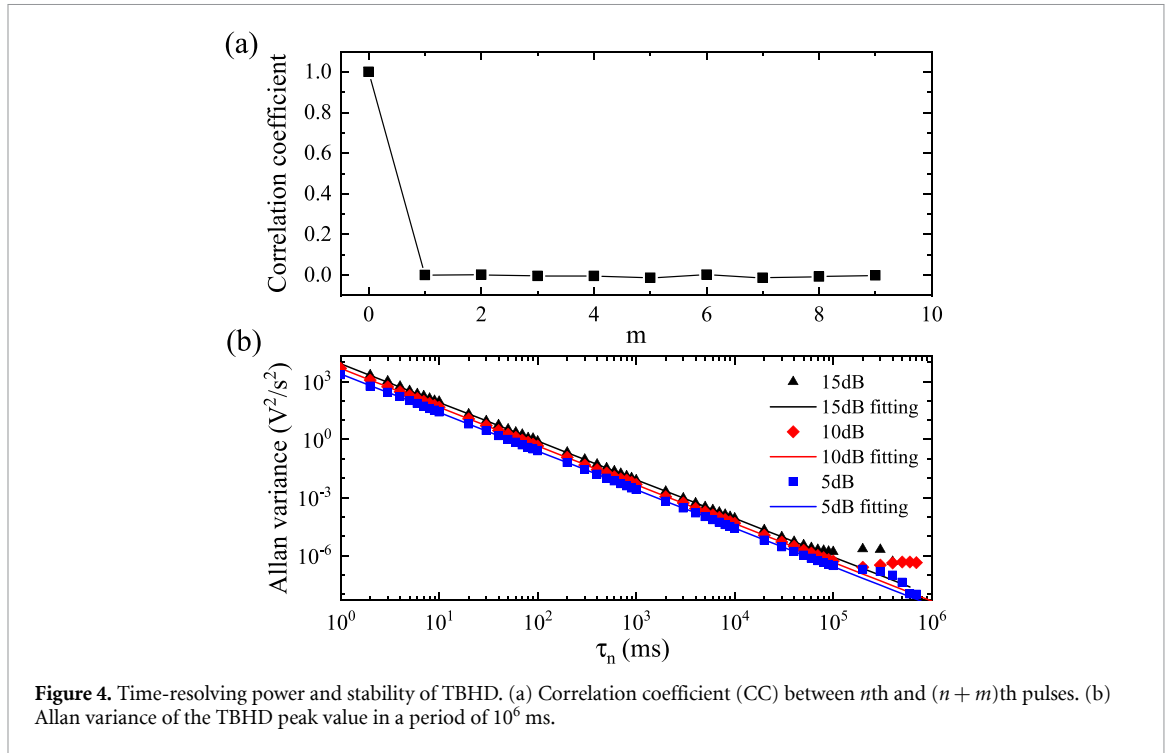
To measure the linearity of the detector, the intensity of the LO beam was tuned and the measurement result was shown in figure 3(b). Multifunction I/O card PCI 6111 was employed to acquire the peak value of the output electronic pulse of TBHD. Here, the voltage range is ±0.5 V, the analog-to-digital converter is 12 bit, and the voltage resolution is 0.25 mV. The green square points represent the measured variance, which is the sum of the shot noise σ^2 and electronic noise. After subtracting the electronic noise variances (black circle points, 7×10^{-5} V^2), the remaining variances shown as red triangle points represent the shot noise variance. A maximum SENR of 19.42 dB is achieved. From equation (5), the gain of TBHD can be calculated as follows

$$G = \sigma \left/ \sqrt{\eta \cdot |\beta|^2} \right. , \qquad (6)$$

where $|\beta|^2$ is the photon number per LO pulse, and $\eta \cdot |\beta|^2$ is photoelectron number per LO pulse. The gain is also the slope of the fitting dash line in figure 3(c). The horizontal and longitudinal coordinate values of the black square points are the square roots of the coordinate values of the red triangle points in figure 3(b). The gain of the detector was 1.25×10^{-5} V photoelectron^{-1}, and the sum of squares of the residual value was 2.27×10^{-36} V^2 in the linear fitting, indicating that TBHD has good linearity.

The correlation coefficient (CC) between adjacent pulses was calculated using equation (7) to check the time-resolving power of TBHD [22, 42, 47]. In the experiment, approximately 5×10^6 output peak points $P(i)(i = 1, 2, \ldots, 5 \times 10^6 + 9)$ were used.

$$\mathrm{CC}(m) = \frac{\langle XY \rangle - \langle X \rangle \langle Y \rangle}{\sqrt{\langle X^2 \rangle - \langle X \rangle^2} \sqrt{\langle Y^2 \rangle - \langle Y \rangle^2}}, \qquad (7)$$

Figure 4. Time-resolving power and stability of TBHD. (a) Correlation coefficient (CC) between nth and $(n+m)$th pulses. (b) Allan variance of the TBHD peak value in a period of 10^6 ms.

where $X(i) = P(i)$ and $Y(i) = P(i+m)$, $(i = 0, 1, \ldots, 5 \times 10^6; m = 0, 1, 2, \ldots, 9)$. Figure 4(a) presents the CC when the pulse repetition rate is 1 MHz. A perfect correlation occurred when $m = 0$, whereas the correlation vanishes for $m \neq 0$. By evaluating the CC, we confirmed that the detector could distinguish individual optical pulses at a repetition rate of 1 MHz, which is enough for the experiment of quantum tomography and CVQKD in the following sections (0.5 MHz).

The stability of TBHD was essential for determining the duration for which the detector could work accurately without calibrating the low-frequency drift of the detector's balance. The photoelectron number per pulse $\eta \cdot |\beta|^2$ was 4.55×10^6 when the SENR was 10 dB, and the corresponding standard deviation of the shot noise was 26.6 mV. Considering the gain of the detector was 1.25×10^{-5} V photoelectron^{-1}, a one-in-a-thousand drift of detector balance could cause a drift of 56.8 mV, which was about 2.1 shot noise units. Thus, a slight imbalance of the TBHD could result in a significant deviation of the output signal. The detector's stability at various time scales was analyzed using Allan variance, which is defined as follows

$$V_{\text{Allan}}^2 (n\tau_0, N) = \frac{1}{2n^2 \tau_0^2 (N - 2n)} \cdot \sum_{i=0}^{N-2n-1} (x_{i+2n} - 2x_{i+n} + x_i)^2, \qquad (8)$$

where x_i is the measured quadrature value, τ_0 ($\tau_0 = 1$ ms) is the time interval between the adjacent sampling points, n is the number of sampling points over time $\tau_n = n \cdot \tau_0$, and N is the total number of samples. All the quadrature values were acquired at 1 kHz at a time scale of 10^6 ms. Afterward, different n was used to calculate the Allan variance at different time scales τ_n, as shown in figure 4(b). The solid lines were fitting lines using the data points for time <1 s. The stability at different SENRs was measured. The time windows T_m for accurate measurement without calibration were 50, 60, and 70 s when the SENRs were 15, 10, and 5 dB, respectively. The detector shows better stability if the SENR is lower.

From the aforementioned analysis, we find that the silicon photonics-integrated TBHD performs well. Its performance is comparable to the TBHD with commercial InGaAs photodiodes, except that the detection efficiency is lower (mainly owing to the 2 dB edge coupling loss). In the future, an edge coupling loss about 1 dB or less is expected to be achieved for our TBHD [23, 48]. Fortunately, there is no need to select the matched photodiodes for TBHD on a chip. In the following sections, quantum tomography and CVQKD experiments using the silicon photonics-integrated TBHD will are demonstrated.

3. Chip TBHD in quantum tomography experiment

As an application of our TBHD detector, we performed quantum tomography of a coherent state by reconstructing its density matrix and Wigner function. Figure 5 presents the scheme for performing quantum tomography using a simple channel. This was also a simple CVQKD setup used to evaluate the excess noise of
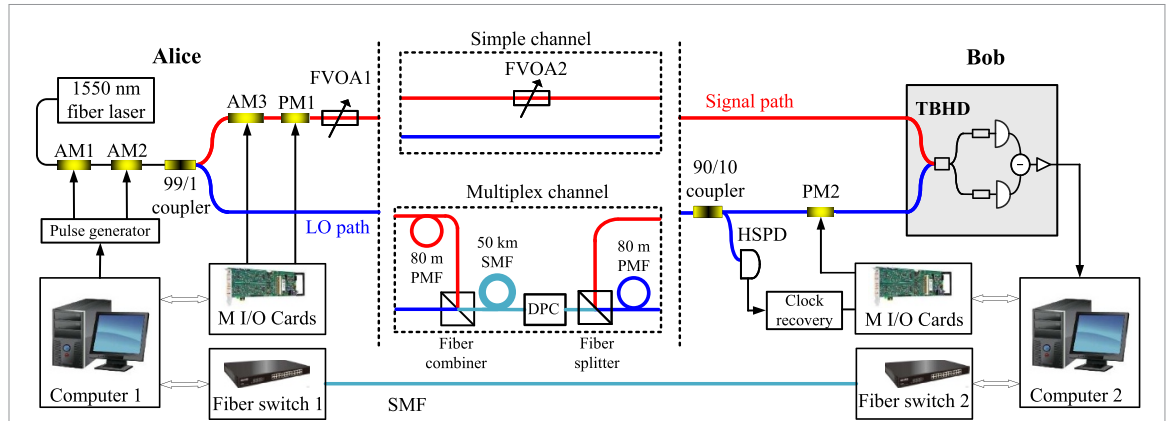
Figure 5. Scheme of the setup to perform quantum tomography and CVQKD. PMF: polarization maintaining fiber; SMF: single mode fiber; DPC: dynamic polarization controller; HSPD: high-speed photodetector; M I/O cards: multifunctional I/O cards.

the system [49]. At the sender, Alice's site, a continuous 1550.14 nm laser beam (Gooch Housego, EM650) was stably modulated into 80 dB high-extinction ratio pulsed beams by two series amplitude modulators (AM1 and AM2, iXblue, MXER-LN-10), and pulse generator (CIQTEK, ASG8100) [50]. The pulse width was 100 ns, and the repetition rate was 0.5 MHz. Subsequently, they were split into signal and LO beams by a 99/1 polarization maintaining fiber coupler. The signal beam could be modulated in the phase space using the amplitude modulator AM3 and phase modulator PM1 (Keyang Photonics, KY-PM-15-300M). The fiber VOAs FVOA1 and FVOA2 could attenuate the intensity of the signal beam to a suitable intensity range. In the simple channel, the signal or LO beam at the sender site was directly connected to the signal or LO beam at the receiver site. At the receiver, Bob's site, a 90/10 polarization maintaining fiber coupler and high-speed photodetector were used to recover the clock signal. Moreover, phase modulator PM2 was used to lock the relative phase and shift the measurement base randomly. The signal and LO beams were guided into the silicon photonics-integrated TBHD. A computer and related multifunction I/O cards (NI, PCI-6111 and PCI-6259) were presented on each site. Two computers were connected by fiber switches (TP-LINK, TL-FC111A/B-60), which were used to transmit classical information.

In the experiment, the sender Alice accurately modulated the signal beam intensity using AM3 and FVOA1 (FVOA2 is set to 0 dB attenuation). Subsequently, the phase was scanned by PM1 from 0 to 2π with an interval of $2\pi/5000$. In each phase, one quadrature value x was acquired. Overall, 5000 samples were used to reconstruct the density matrix $\hat{\rho}$ with the iteration operator $\hat{R}$ using the maximum likelihood method [1]. Figure 6(a) presents the reconstructed density matrix. The iteration expression is shown in equation (9).

$$\hat{\rho}^{(k+1)} = N\left[\hat{R}\left(\hat{\rho}^{(k)}\right)\cdot\hat{\rho}^{(k)}\cdot\hat{R}\left(\hat{\rho}^{(k)}\right)\right]. \tag{9}$$

Using the reconstructed density matrix, an average photon number $\langle n\rangle = \sum n\cdot\rho_{nn} = 1.08$ was calculated from the measured photon number distribution. It corresponds to the coherent state $|\alpha\rangle = 1.04$. The comparison of the reconstructed density matrix with that of an ideal coherent state $|\alpha\rangle = 1.04$ yields a state preparation fidelity F

$$F = \langle\alpha|\hat{\rho}|\alpha\rangle = 99.97\%. \tag{10}$$
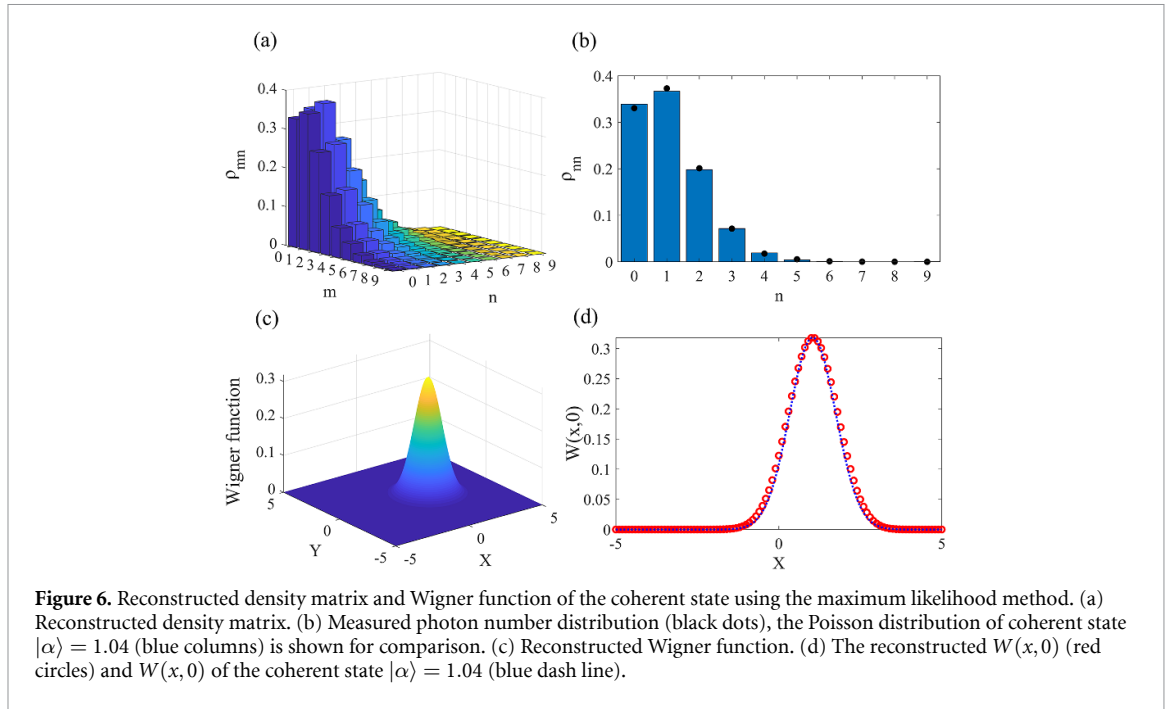
Figure 6(b) presents the comparison of the measured photon number distribution with a Poisson distribution of the coherent state $|\alpha\rangle = 1.04$. Considering the detection efficiency $\eta = 0.38$ at the receiver's side. The coherent state prepared by Alice is $|\alpha\rangle = 1.69$.

Based on the calculated density matrix $\hat{\rho}$, the Wigner function can be calculated using the following equation

$$W(x,y) = tr\left[\hat{\rho}\cdot\exp\left[-2\left(\hat{a}^\dagger - \gamma^*\right)\left(\hat{a} - \gamma\right)\right]/\pi\right], \tag{11}$$

where $\hat{a}^\dagger$ and $\hat{a}$ are the creation and annihilation operators, and γ is defined as $\gamma = x + iy$. Figure 6(c) presents the reconstructed Wigner function. In figure 6(d), the red circle line presents the reconstructed $W(x,0)$, which coincides well with $W(x,0)$ of the coherent state $|\alpha\rangle = 1.04$. From the aforementioned results, we can infer that the silicon photonics-integrated TBHD could reliably measure and reconstruct the quantum states. In the future, we will apply our silicon photonics-integrated TBHD to characterize the non-classical quantum states such as squeezing states and entangled states.

Figure 6. Reconstructed density matrix and Wigner function of the coherent state using the maximum likelihood method. (a) Reconstructed density matrix. (b) Measured photon number distribution (black dots), the Poisson distribution of coherent state $|\alpha\rangle = 1.04$ (blue columns) is shown for comparison. (c) Reconstructed Wigner function. (d) The reconstructed $W(x, 0)$ (red circles) and $W(x, 0)$ of the coherent state $|\alpha\rangle = 1.04$ (blue dash line).

4. Chip TBHD in CVQKD experiment

The main aim of the CVQKD experiment was to demonstrate that excess noise measured using silicon photonics-integrated TBHD could be low enough to be below the threshold for key generation. The experiment setup is shown in figure 5.

In the CVQKD experiment, the GG02 protocol was utilized, and all the variances were normalized to the shot noise. At the sender Alice's site, the Gaussian modulation variance was calibrated as $V_A = 5.8$, and the electronics noise was $\upsilon_e = 0.1$. Moreover, a reverse reconciliation efficiency of $\beta = 0.98$ was used. The data block containing data samples of 10^8 was used to evaluate the parameters and extract the secret keys. In the experiment, transmission losses of 5 and 10 dB (set by FVOA2) in the simple channel and 50 km single-mode fiber in the multiplexing channel were used. In the multiplexing channel, 80 m polarization maintaining fibers were designed for time multiplexing, and the fiber combiner and splitter were used for polarization multiplexing. The multiplexing channel was used to prevent the interference of the signal and LO beams and the fast change of the relative phase between the two beams. The dynamic polarization controller (General Photonics, PCD-M02-4X-7-FC/APC) was used to rotate the polarization of the combined signal and LO pulses back to linear polarization, and then they could be split by the fiber splitter. The excess noises and corresponding secret key rates of the CVQKD system were measured and depicted in figure 7.

In figures 7(a)–(c), the solid points represent the experimental results of the CVQKD system based on the silicon photonics-integrated TBHD. For comparison, the hollow points with the same shape represent the experimental results conducted on the fiber-based TBHD with a commercial InGaAs photodiode in figures 7(d)–(f). In CVQKD, the variance of data measured by receiver Bob V_B can be expressed as

$$V_B = \eta T(V_A + \varepsilon_a) + \eta T \varepsilon_l + \varepsilon_b + N_0 + \upsilon_e, \tag{12}$$

where ε_a is the excess noise generated at Alice's site, ε_l is the excess noise introduced by the quantum transmission channel and is normalized to the input port of the quantum channel, ε_b is the excess noise generated at Bob's site, N_0 is the shot noise with value of one, and T represents the quantum channel loss.
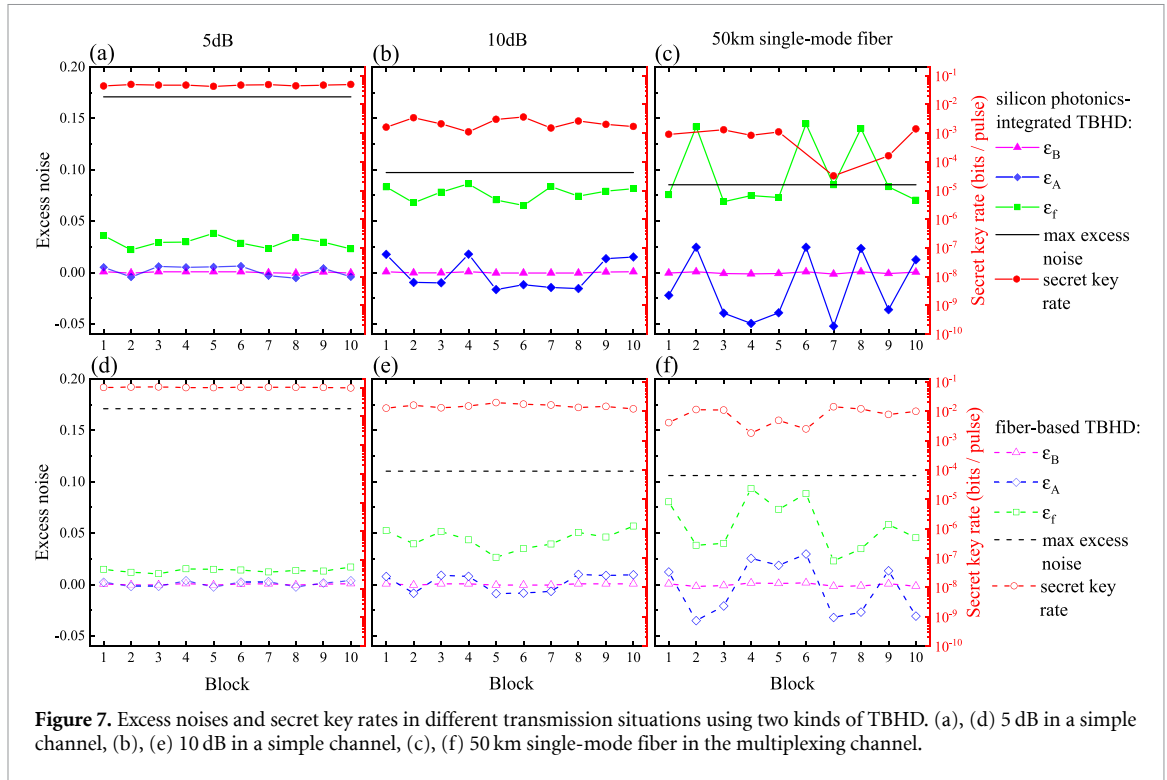
The measured excess noise at Bob's site ε_B can be calculated by

$$\varepsilon_B = \eta T(\varepsilon_a + \varepsilon_l) + \varepsilon_b = V_B - \eta T V_A - N_0 - \upsilon_e, \tag{13}$$

The excess noise ε_A normalized to the input port of the quantum channel is given by

$$\varepsilon_A = \varepsilon_B / \eta T = (\varepsilon_a + \varepsilon_l) + \varepsilon_b / \eta T = (V_B - N_0 - \upsilon_e) / \eta T - V_A. \tag{14}$$

In CVQKD experiment, we only evaluate the excess noises ε_A and ε_B, it is difficult to evaluate the excess noises ε_a, ε_l and ε_b separately. Due to the term $\varepsilon_b / \eta T$ from equation (14), the magnification of the excess

Figure 7. Excess noises and secret key rates in different transmission situations using two kinds of TBHD. (a), (d) 5 dB in a simple channel, (b), (e) 10 dB in a simple channel, (c), (f) 50 km single-mode fiber in the multiplexing channel.

noise ε_A will become larger when the transmission loss is larger. When the transmission channel was 5 dB loss, 10 dB loss, and 50 km fiber, the excess noise could be controlled to 0.029 ± 0.009, 0.077 ± 0.012, and 0.096 ± 0.049. The secret key rate is very sensitive to the excess noise. Thus, from 5 dB to 10 dB, and 50 km, the excess noise ε_A and its fluctuation become larger. At the same time, the fluctuation of secret key rates becomes more obviously [51–53].

Figures 7(a) and (d) depict the experimental results using silicon photonics-integrated TBHD and fiber-based TBHD respectively in which the total transmission loss was 5 dB in the simple channel. The solid and hollow pink triangle points represent the excess noise ε_B, they nearly overlapped with the solid and hollow blue diamond points which represent the excess noise ε_A. There was negative excess noise of ε_B, mainly due to the statistical effect of finite samples. The solid and hollow green square points represent the excess noise ε_f considering the finite-size effect

$$\varepsilon_f = \varepsilon_A + z_{\delta_{PE/2}} \frac{(1 + \eta T \varepsilon + \upsilon_e)\sqrt{2}}{\eta T \sqrt{m}}, \tag{15}$$

where $z_{\delta_{PE/2}} = \sqrt{2} erf^{-1}(1 - \delta_{PE})$ and m is the amount of data used to estimate the parameters. Each data block contains $N = 10^8$ data points. The optimum ratio of data used to evaluate the parameters is $r = m/N$, which is 0.1. The final secret key rate of the system is calculated using equation (16). The results are drawn as red circle points.

$$K_r^f = \frac{n}{N}\left(\beta I_{AB} - \chi_{BE}^{\delta_{PE}} - \Delta(n)\right), \tag{16}$$

where $n = N - m$ represents the number of signals used to extract the secret keys. I_{AB} is the Shannon mutual information between Alice and Bob. β is the reverse reconciliation efficiency. $\chi_{BE}^{\delta_{PE}}$ represents the maximum of the Holevo information compatible with the statistics, except with the probability $\delta_{PE} = 10^{-10}$. Moreover, $\Delta(n)$ is a correction term for the achievable mutual information in the finite case [52, 54].

Figures 7(b) and (e) show the excess noises and secret key rates when the transmission loss was 10 dB in the simple channel. Figures 7(c) and (f) plot the corresponding excess noises and secret key rates when transmission channel was 50 km single mode fiber in the multiplexed channel. Considering the dynamic polarization controller and fiber splitter losses, the detection efficiency of the receiver's TBHD on the chip changed from 0.38 to 0.28. Correspondingly, the detection efficiency of fiber-based TBHD changed from 0.72 to 0.53. The black solid and dashed lines in each subfigure represent the maximum excess noise that can be endured by the CVQKD system. The excess noises ε_f of some blocks exceeded the maximum allowable excess noise level (figure 7(c)), and their secret key rates dropped to zero. The excess noises ε_B in different

transmission losses were nearly the same. The excess noises ε_A were different mainly owing to the difference in the transmission loss T and detection efficiency η. For example, the excess noises using silicon photonics-integrated TBHD were approximately double that of the fiber-based TBHD in the simple channel, mainly because the detection efficiency of the former was half that of the latter. Thus, the performances of the two kinds of TBHD were similar in evaluating the excess noise except for the detection efficiency.

From the aforementioned results, we can conclude that the silicon photonics-integrated TBHD was suitable for the CVQKD system. Additionally, the excess noise could be controlled to a low level, as in the CVQKD system with fiber-based TBHD. Because the excess noise ε_A was normalized to the input port of the transmission channel, it increased when the value of ηT decreased. Furthermore, the coupling loss and quantum efficiency that affect the detection efficiency should be further optimized to improve the performance of the TBHD on a chip.

5. Conclusions

We designed and demonstrated a silicon photonics-integrated TBHD based on industry-standard SOI technology. The structures and characteristics are presented in detail. The signal and LO beams could transmit into the chip using packaged edge coupler technology with an insertion loss of approximately 2 dB. Using VOA based on the p–i–n phase modulator and Ge photodiodes with tunable bias voltages, a CMRR of 86.9 dB could be achieved. The charge and shaping amplifiers using the low-noise ADA4817 and OPA847 could ensure that a maximum SENR of 19.42 dB was achieved. The TBHD could output a Gaussian-shaped pulse with a full pulse width of 200 ns. The mean value of the shot noise could be controlled in the range of ± 2 mV automatically. The detector had good linearity and a gain of 12.5 μV photoelectron^{-1}. The stability of TBHD at different SENRs was measured, and the detector showed better stability if the SENR was lower. Using the TBHD, a quantum tomography of a coherent state $|\alpha\rangle = 1.04$ was conducted, and 99.97% fidelity was achieved. To demonstrate the performance of the integrated TBHD in the CVQKD system, the CVQKD setup with both simple and multiplexing channels was designed.

Our results indicate that the silicon photonics-integrated TBHD could perform as well as the TBHD based on the commercial InGaAs photodiode. Because the two photodiodes were fabricated in the same wafer using the same procedures, their characteristics were considerably similar. Therefore, a high CMRR could be achieved, and there was no need to select photodiodes on chips. For further study, it is expected that the whole CVQKD system could be integrated into the chip. In the receiver, the main challenge was integrating the TBHD on the chip, which has been verified in our work. An edge coupling loss about 1 dB or less is expected to be achieved in the future [23, 48]. Additionally, a whole decoder using BB84 protocol with TBHD, which is compatible with single photon technology, may be realized on a single silicon photonics chip [45].

Overall, we designed and demonstrated silicon photonics-integrated TBHD, which performed well in quantum tomography and CVQKD experiments. Furthermore, it is expected that the proposed technologies can be used in silicon photonics-integrated CVQKD system and silicon photonics-integrated BB84 heterodyne system.

Data availability statement

All data that support the findings of this study are included within the article (and any supplementary files).

Acknowledgments

Appendix A. VOAs based on MZI structures

To balance 50/50 couplers, the authors of [40] used two 50/50 couplers and a thermal phase modulator between them, which is equivalent to a 2×2 MZI, as shown in figure A1(a). Compared with the structure of our TBHD with one 50/50 MMI coupler, the additive 2×2 50/50 MMI coupler will introduce approximately
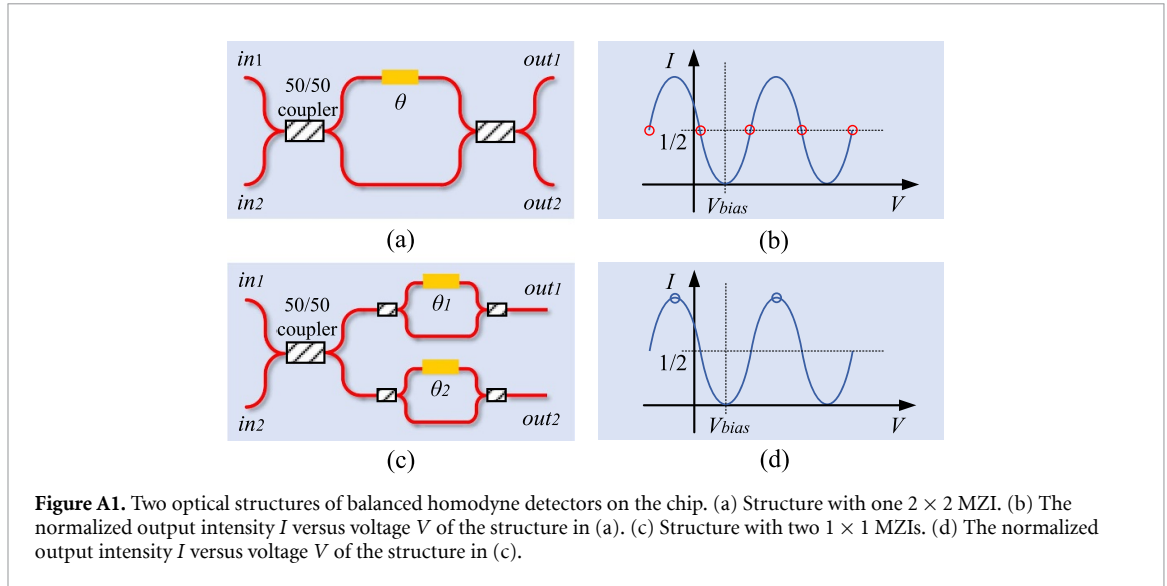
Figure A1. Two optical structures of balanced homodyne detectors on the chip. (a) Structure with one 2×2 MZI. (b) The normalized output intensity I versus voltage V of the structure in (a). (c) Structure with two 1×1 MZIs. (d) The normalized output intensity I versus voltage V of the structure in (c).

0.3–0.7 dB loss [23]. The input ports are in_1 and in_2, and the output ports are out_1 and out_2. When a laser beam is injected into one input port of the MZI, the normalized output light intensities are given by

$$I = \frac{1 \pm \cos\theta}{2}. \tag{A1}$$

The relative phase θ can be controlled by applied voltage V. Considering the bias voltage V_{bias}, the normalized output intensities I can be transformed into the following equation

$$I = \left(1 \pm \cos\left[(V - V_{\text{bias}}) \cdot \pi / V_\pi\right]\right)/2, \tag{A2}$$

where the bias voltage V_{bias} corresponds to phase θ_{bias}. Their relationship is drawn in figure A1(b). When the light intensities of the output ports out_1 and out_2 are balance, the relative phase θ are $\pi/2 \pm n\pi$. They correspond to the red circle points in figure A1(b), and we note them work points which have the maximum gradient.

The structure in [41] includes one thermal MZI modulator in each output path as shown in figure A1(c). The additive two 1×2 50/50 MMI couplers will introduce approximately 0.5–0.6 dB loss [23]. The normalized output intensity I of each output port can be represented as equation (A3). The work points of each MZI are around the blue circles (vertex points), as shown in figure A1(d).

$$I = \frac{1 + \cos\theta_i}{2} \ (i = 1, 2). \tag{A3}$$

Due to the MZI structures are used, the bias voltage should be scanned and applied to balance the intensities of the two beams. However, the bias voltage will drift mainly due to temperature variance. Then the bias voltage should be scanned and applied again and again to make their work point stable. When the balanced homodyne detectors with MZI structures are used in the CVQKD system, a long running time is required. Thus, a lock technology is necessary to achieve balanced and stable running state. Since the curve around each red work point in figure A1(b) is monotonous, a simple lock technology can be designed. However, the maximum gradient position makes it more unstable than the blue work point in figure A1(d). Conversely, the curve around each blue work point is not monotonous, the lock technology will be harder to realize.

Appendix B. CMRR and tuning precision of TBHD

The measurement of CMRR of TBHD differs from that of FBHD. The CMRR of the FBHD can be measured directly using a radio frequency spectrum analyzer with the sideband method [55]. However, this method is not suitable for TBHD. The CMRR of TBHD can be calculated by the following equation

$$\text{CMRR} = 20 \cdot \log_{10}\left|\frac{G_{\text{DM}}}{G_{\text{CM}}}\right|, \tag{B1}$$

where G_{DM} is the differential mode magnification, and G_{CM} is the /common mode magnification. G_{DM} is also the gain G of the charge and shaping amplifiers, and it can be calculated using the following equation

$$\sigma^2 = G_{DM}^2 \cdot \eta \cdot |\beta|^2. \tag{B2}$$

When we measure G_{CM}, the two output paths of TBHD should be tuned to balance. However, even if the light intensities of two paths are equivalent, the responses of two photodiodes may be different. Thus, the subtracted photoelectrons Δ will generate a voltage μ which is the non-zero mean value of shot noise. Their relationship can be expressed as

$$\mu = G_{DM} \cdot \Delta. \tag{B3}$$

The relationship of the mean voltage μ and input photoelectron number per pulse $\eta \cdot |\beta|^2$ can be expressed as follows

$$\mu = G_{CM} \cdot \eta \cdot |\beta|^2. \tag{B4}$$

Tuning precision is the minimum tunable normalized output intensity I of VOA when a high resolution voltage is applied. The needed tuning precision is depended on the photoelectron number per LO pulse. Generally, when the photoelectron number per pulse is 10^8, a CMRR larger than 80 dB and a tuning precision ΔI_{tp} less than 1×10^{-4} are needed. The reason for this will be shown as follows.

The mean value of the output shot noise variance μ can be calculated using equations (B3) and (B4). It means that

$$\mu = G_{DM} \cdot \Delta = G_{CM} \cdot \eta \cdot |\beta|^2. \tag{B5}$$

In addition, the standard deviation σ can be calculated using equation (B2) as $\sigma = G_{DM} \cdot \sqrt{\eta \cdot |\beta|^2}$. Generally, to make the TBHD run in a well balanced state, the mean value μ should be less than or equal to standard deviation σ. When $\eta \cdot |\beta|^2$ is 10^8, the required CMRR can be calculated as follows

$$\sigma \geqslant \mu,$$
$$G_{DM} \cdot \sqrt{\eta \cdot |\beta|^2} \geqslant G_{CM} \cdot \eta \cdot |\beta|^2,$$
$$\text{CMRR} = 20 \cdot \log_{10} \left| \frac{G_{DM}}{G_{CM}} \right| \geqslant 20 \cdot \log_{10} \left(\sqrt{\eta \cdot |\beta|^2} \right) = 80 \, (\text{dB}). \tag{B6}$$

In the experiment, the mean value is the smaller the better. So the CMRR is the higher the better. According to the equations (B5) and (B6), the subtracted photoelectrons value Δ satisfies the following equation

$$\frac{G_{DM}}{G_{CM}} = \frac{\eta \cdot |\beta|^2}{\Delta} \geqslant 10^4 \Rightarrow \Delta \leqslant 10^4. \tag{B7}$$

In this case, the balance degree BD, which is defined as the subtracted photoelectrons Δ divided by the total photoelectrons $\eta \cdot |\beta|^2$ of the two photodiodes, can be described by

$$\text{BD} = \frac{\Delta}{\eta \cdot |\beta|^2} \leqslant 1 \times 10^{-4}. \tag{B8}$$

It means that a tuning precision $\Delta I_{tp} \leqslant BD \leqslant 1 \times 10^{-4}$ is needed.

To calculate the needed voltage resolution ΔV_{vr}, the experimental results of figure 2(a) are presented in table B1. The normalized output intensities are noted as $I_i \, (i = 1, 2, \ldots)$, and the applied forward voltages are noted as $V_i \, (i = 1, 2, \ldots)$. For a tuning precision ΔI_{tp}, the required voltage resolution ΔV_{vr} can be calculated using the following equation

$$\frac{I_{i+1} - I_i}{V_{i+1} - V_i} = \frac{\Delta I_i}{\Delta V_i} = \frac{\Delta I_{tp}}{\Delta V_{vr}}. \tag{B9}$$

The attenuated normalized output intensities can be calculated by $1 - I$.

In the experiment, the photoelectron number was 4.82×10^6 /pulse when the SENR was 10.3 dB. The mean value of the output variance was $\mu = 0.00274 \, \text{V}$. The gain G_{CM} could be calculated as $5.64 \times 10^{-10} \, \text{V photoelectron}^{-1}$. Finally, the CMRR could be calculated as 86.9 dB. In this case, a tuning precision 4.55×10^{-4} is needed and a 66.83 dB CMRR is needed.

Table B1. The normalized output intensities and currents versus the forward voltages.

i	Forward voltage (V)	VOA$_1$		VOA$_2$	
		I (%)	Current (mA)	I (%)	Current (mA)
1	0	100	0	100	0
2	0.6	100	0	100	0
3	0.65	99.6	0	99.3	0
4	0.7	99.3	0	99.0	0
5	0.75	98.9	0.01	98.7	0.01
6	0.8	94.7	0.06	93.5	0.06
7	0.85	84.0	0.24	83.1	0.24
8	0.9	66.3	0.84	65.5	0.88
9	0.95	50.5	2.14	49.3	2.18
10	1	35.9	4.12	34.9	4.27
11	1.05	23.9	6.64	23.3	6.79
12	1.1	16.4	9.56	16.0	9.74
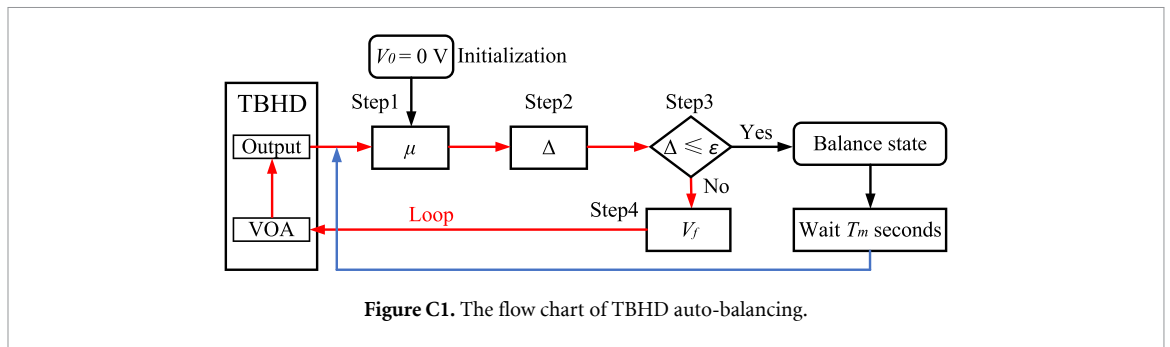
Figure C1. The flow chart of TBHD auto-balancing.

Appendix C. The method of auto-balancing the TBHD

Figure C1 presents the TBHD auto-balancing flow chart. In the beginning, forward voltage value $V_0 = 0\,\mathrm{V}$ should be initialized. All the steps in a loop are depicted as follows:

Step 1. Acquire the peak values of TBHD using a data acquisition card to calculate the mean value μ.

Step 2. According to the mean value μ and G_{DM}, the value Δ can be evaluated by the following equation

$$\mu = G_{\mathrm{DM}} \cdot \Delta. \tag{C1}$$

Step 3. Compare $|\Delta|$ and threshold value ε. If $|\Delta| \leqslant \varepsilon$, the TBHD is in a balanced state, and there is no need to feedback. If $|\Delta| > \varepsilon$, the TBHD is unbalanced. The attenuated normalized output intensity is calculated by

$$1 - I = \frac{|\Delta|}{\eta|\beta|^2/2}, \tag{C2}$$

where $\eta|\beta|^2/2$ is approximately the photoelectron number of one photodiode. Due to $|\Delta| \ll \eta|\beta|^2/2$, the variance of $\eta|\beta|^2/2$ is negligible. Using table B1, the voltage resolution ΔV_i can be determined by $I_i \leqslant I \leqslant I_{i+1}$. Then, the feedback signal V_n of nth loop can be calculated using the follow equation

$$V_n = V_{n-1} + P(\Delta V_i, \Delta) \cdot \Delta V_i, \tag{C3}$$

where P is the proportional gain which can be tuned according to ΔV_i, and it is positive or negative depends on Δ.

Step 4. Apply the feedback signal on the VOA and enter the step 1 again. In the experiment, one VOA is enough to auto-balance the TBHD. The feedback voltage is usually applied on the VOA in the path with a higher transmission efficiency.

Usually, after 20 loops the TBHD will reach a balanced state. After achieving the balance, the auto-balancing procedure system will re-enter the loop after waiting time of T_{m}, which is the accurate measurement time without calibration.

References

[1] Lvovsky A I and Raymer M G 2009 Continuous-variable optical quantum-state tomography *Rev. Mod. Phys.* **81** 299–332

[2] Tiunov E S, Tiunova (Vyborova) V V, Ulanov A E, Lvovsky A I and Fedorov A K 2020 Experimental quantum homodyne tomography via machine learning *Optica* **7** 448–54

[3] Smithey D T, Beck M, Raymer M G and Faridani A 1993 Measurement of the wigner distribution and the density matrix of a light mode using optical homodyne tomography: application to squeezed states and the vacuum *Phys. Rev. Lett.* **70** 1244–7

[4] Breitenbach G, Schiller S and Mlynek J 1997 Measurement of the quantum states of squeezed light *Nature* **387** 471–5

[5] Vasilyev M, Choi S K, Kumar P and D'Ariano G M 2000 Tomographic measurement of joint photon statistics of the twin-beam quantum state *Phys. Rev. Lett.* **84** 2354

[6] Grosshans F and Grangier P 2002 Continuous variable quantum cryptography using coherent states *Phys. Rev. Lett.* **88** 057902

[7] Silberhorn C, Ralph T C, Lütkenhaus N and Leuchs G 2002 Continuous variable quantum cryptography: beating the 3 dB loss limit *Phys. Rev. Lett.* **89** 167901

[8] Grosshans F, Van Assche G, Wenger J, Brouri R, Cerf N J and Grangier P 2003 Quantum key distribution using Gaussian-modulated coherent states *Nature* **421** 238–41

[9] Lodewyck J *et al* 2007 Quantum key distribution over 25 km with an all-fiber continuous-variable system *Phys. Rev. A* **76** 042305

[10] Jouguet P, Kunz-Jacques S, Leverrier A, Grangier P and Diamanti E 2013 Experimental demonstration of long-distance continuous-variable quantum key distribution *Nat. photon.* **7** 378–81

[11] Zhang Y, Chen Z, Pirandola S, Wang X, Zhou C, Chu B, Zhao Y, Xu B, Yu S and Guo H 2020 Long-distance continuous-variable quantum key distribution over 202.81 km of fiber *Phys. Rev. Lett.* **125** 010502

[12] Pan Y, Wang H, Shao Y, Pi Y, Li Y, Liu B, Huang W and Xu B 2022 Experimental demonstration of high-rate discrete-modulated continuous-variable quantum key distribution system *Opt. Lett.* **47** 3307–10

[13] Tian Y, Wang P, Liu J, Du S, Liu W, Lu Z, Wang X and Li Y 2022 Experimental demonstration of continuous-variable measurement-device-independent quantum key distribution over optical fiber *Optica* **9** 492–500

[14] Tian Y, Zhang Y, Liu S, Wang P, Lu Z, Wang X and Li Y 2023 High-performance long-distance discrete-modulation continuous-variable quantum key distribution *Opt. Lett.* **48** 2953–6

[15] Wang X, Liu W, Wang P and Li Y 2017 Experimental study on all-fiber-based unidimensional continuous-variable quantum key distribution *Phys. Rev. A* **95** 062330

[16] Huang P, Wang T, Chen R, Wang P, Zhou Y and Zeng G 2021 Experimental continuous-variable quantum key distribution using a thermal source *New J. Phys.* **23** 113028

[17] Du S, Wang P, Liu J, Tian Y and Li Y 2023 Continuous variable quantum key distribution with a shared partially characterized entangled source *Photon. Res.* **11** 463–75

[18] Zavatta A, Viciani S and Bellini M 2004 Quantum-to-classical transition with single-photon-added coherent states of light *Science* **306** 660–2

[19] Qi B, Lougovski P and Williams B P 2020 Characterizing photon number statistics using conjugate optical homodyne detection *Opt. Express* **28** 2276–90

[20] Lvovsky A I, Hansen H, Aichele T, Benson O, Mlynek J and Schiller S 2001 Quantum state reconstruction of the single-photon fock state *Phys. Rev. Lett.* **87** 050402

[21] Hansen H, Aichele T, Hettich C, Lodahl P, Lvovsky A, Mlynek J and Schiller S 2001 Ultrasensitive pulsed, balanced homodyne detector: application to time-domain quantum measurements *Opt. Lett.* **26** 1714–6

[22] Du S, Li Z, Liu W, Wang X and Li Y 2018 High-speed time-domain balanced homodyne detector for nanosecond optical field applications *J. Opt. Soc. Am. B* **35** 481–6

[23] Siew S Y *et al* 2021 Review of silicon photonics technology and platform development *J. Light. Technol.* **39** 4374–89

[24] Diamanti E, Lo H K, Qi B and Yuan Z 2016 Practical challenges in quantum key distribution *npj Quantum Inf.* **2** 1–12

[25] Wang J, Sciarrino F, Laing A and Thompson M G 2020 Integrated photonic quantum technologies *Nat. Photon.* **14** 273–84

[26] Ma C, Sacher W D, Tang Z, Mikkelsen J C, Yang Y, Xu F, Thiessen T, Lo H K and Poon J K 2016 Silicon photonic transmitter for polarization-encoded quantum key distribution *Optica* **3** 1274–8

[27] Sibson P, Kennard J E, Stanisic S, Erven C, O'Brien J L and Thompson M G 2017 Integrated silicon photonics for high-speed quantum key distribution *Optica* **4** 172–7

[28] Sibson P *et al* 2017 Chip-based quantum key distribution *Nat. Commun.* **8** 1–6

[29] Wang C Y *et al* 2019 Integrated measurement server for measurement-device-independent quantum key distribution network *Opt. Express* **27** 5982–9

[30] Geng W, Zhang C, Zheng Y, He J, Zhou C and Kong Y 2019 Stable quantum key distribution using a silicon photonic transceiver *Opt. Express* **27** 29045–54

[31] Wei K, Li W, Tan H, Li Y, Min H, Zhang W J, Li H, You L, Wang Z and Jiang X 2020 High-speed measurement-device-independent quantum key distribution with integrated silicon photonics *Phys. Rev. X* **10** 031030

[32] Cao L *et al* 2020 Chip-based measurement-device-independent quantum key distribution using integrated silicon photonic systems *Phys. Rev. Appl.* **14** 011001

[33] Kong L, Li Z, Li C, Cao L, Xing Z, Cao J, Wang Y, Cai X and Zhou X 2020 Photonic integrated quantum key distribution receiver for multiple users *Opt. Express* **28** 18449–55

[34] Paraiso T K, Roger T, Marangon D G, De Marco I, Sanzaro M, Woodward R I, Dynes J F, Yuan Z and Shields A J 2021 A photonic integrated quantum secure communication system *Nat. Photon.* **15** 850–6

[35] Beutel F, Gehring H, Wolff M A, Schuck C and Pernice W 2021 Detector-integrated on-chip QKD receiver for GHz clock rates *NPJ Quantum Inf.* **7** 1–8

[36] Du Y, Zhu X, Hua X, Zhao Z, Hu X, Qian Y, Xiao X and Wei K 2023 Silicon-based decoder for polarization-encoding quantum key distribution *Chip* **2** 100039

[37] Zhang G *et al* 2019 An integrated silicon photonic chip platform for continuous-variable quantum key distribution *Nat. Photon.* **13** 839–42

[38] Wang X, Jia Y, Guo X, Liu J, Wang S, Liu W, Sun F, Zou J and Li Y 2022 Silicon photonics integrated dynamic polarization controller *Chin. Opt. Lett.* **20** 041301

[39] Li L, Wang T, Li X, Huang P, Guo Y, Lu L, Zhou L and Zeng G 2023 Continuous-variable quantum key distribution with on-chip light sources *Photon. Res.* **11** 504–16

[40] Tasker J F, Frazer J, Ferranti G, Allen E J, Brunel L F, Tanzilli S, D'Auria V and Matthews J C 2021 Silicon photonics interfaced with integrated electronics for 9 GHz measurement of squeezed light *Nat. Photon.* **15** 11–15

[41] Bruynsteen C, Vanhoecke M, Bauwelinck J and Yin X 2021 Integrated balanced homodyne photonic–electronic detector for beyond 20 GHz shot-noise-limited measurements *Optica* **8** 1146–52

[42] Chi Y M, Qi B, Zhu W, Qian L, Lo H K, Youn S H, Lvovsky A and Tian L 2011 A balanced homodyne detector for high-rate Gaussian-modulated coherent-state quantum key distribution *New J. Phys.* **13** 013003

[43] Wang S, Xiang X, Zhou C, Zhai Y, Quan R, Wang M, Hou F, Zhang S, Dong R and Liu T 2017 Simulation of high SNR photodetector with L-C coupling and transimpedance amplifier circuit and its verification *Rev. Sci. Instrum.* **88** 013107

[44] Bennett C H and Brassard G 1984 Quantum cryptography: public key distribution and coin tossing *Proc. IEEE Int. Conf. on Computers*

[45] Qi B 2021 Bennett-brassard 1984 quantum key distribution using conjugate homodyne detection *Phys. Rev.* A **103** 012606

[46] Ramos M, Pinto A and Silva N 2022 Polarization based discrete variables quantum key distribution via conjugated homodyne detection *Sci. Rep.* **12** 6135

[47] Okubo R, Hirano M, Zhang Y and Hirano T 2008 Pulse-resolved measurement of quadrature phase amplitudes of squeezed pulse trains at a repetition rate of 76 MHz *Opt. Lett.* **33** 1458–60

[48] Cheben P, Schmid J H, Wang S, Xu D X, Vachon M, Janz S, Lapointe J, Painchaud Y and Picard M J 2015 Broadband polarization independent nanophotonic coupler for silicon waveguides with ultra-high efficiency *Opt. Express* **23** 22553–63

[49] Lodewyck J, Debuisschert T, Tualle-Brouri R and Grangier P 2005 Controlling excess noise in fiber-optics continuous-variable quantum key distribution *Phys. Rev.* A **72** 050303

[50] Wang X, Liu J, Li X and Li Y 2015 Generation of stable and high extinction ratio light pulses for continuous variable quantum key distribution *IEEE J. Quantum Electron.* **51** 1–6

[51] Liu W, Wang X, Wang N, Du S and Li Y 2017 Imperfect state preparation in continuous-variable quantum key distribution *Phys. Rev.* A **96** 042312

[52] Leverrier A, Grosshans F and Grangier P 2010 Finite-size analysis of a continuous-variable quantum key distribution *Phys. Rev.* A **81** 062343

[53] Wang X, Guo S, Wang P, Liu W and Li Y 2019 Realistic rate-distance limit of continuous-variable quantum key distribution *Opt. Express* **27** 13372–86

[54] Wang P, Wang X, Li J and Li Y 2017 Finite-size analysis of unidimensional continuous-variable quantum key distribution under realistic conditions *Opt. Express* **25** 27995–8009

[55] Jin X, Su J, Zheng Y, Chen C, Wang W and Peng K 2015 Balanced homodyne detection with high common mode rejection ratio based on parameter compensation of two arbitrary photodiodes *Opt. Express* **23** 23859–66